Available online at www.sciencedirect.com

ScienceDirect

Procedia Computer Science 108C (2017) 2008–2017

Procedia Computer Science

International Conference on Computational Science, ICCS 2017, 12-14 June 2017, Zurich, Switzerland

DNS of the wall effect on the motion of bubble swarms

Néstor Balcázar[1], Jesús Castro[1], Joaquim Rigola[1], and Assensi Oliva[1]

Heat and Mass Transfer Technological Center (CTTC)
Universitat Politècnica de Catalunya-BarcelonaTech
ETSEIAT, Colom 11, 08222 Terrassa (Barcelona), Spain
web page: http://www.cttc.upc.edu
nestor@cttc.upc.edu, cttc@cttc.upc.edu

Abstract

This paper presents a numerical study of the gravity-driven motion of single bubbles and bubble swarms through a vertical channel, using High-Performance Computing (HPC) and Direct Numerical Simulation (DNS) of the Navier-Stokes equations. A systematic study of the wall effect on the motion of single deformable bubbles is carried out for confinement ratios $CR = \{2, 4, 6\}$ in both circular and square channels, for a broad range of flow conditions. Then, the rising motion of a swarm of deformable bubbles in a vertical channel is researched, for void fractions $\alpha = \{8.3\%, 10.4\%, 12.5\%\}$ and $CR = \{4, 6\}$. These simulations are carried out in the framework of a novel multiple marker interface capturing approach, where a conservative level-set function is used to represent each bubble. This method avoids the numerical and potentially unphysical coalescence of the bubbles, allowing for the collision of the fluid particles as well as long time simulations of bubbly flows. Present simulations are performed in a periodic vertical domain discretized by 2×10^6 control volumes (CVs) up to 16.6×10^6 CVs, distributed in 128 up to 2048 processors. The collective and individual behavior of the bubbles are analyzed in detail.

Peer-review under responsibility of the scientific committee of the International Conference on Computational Science

Keywords: bubble swarm, level-set method, unstructured meshes, DNS, HPC

1 Introduction

Bubbly flows are relevant in both natural and industrial processes. Some examples can be found in technological applications, which include steam generators in nuclear plants, unit operations of the chemical engineering, such as bubble reactors and absorption columns, where the bubbles provide a high interfacial area per unit volume, allowing for high heat and mass transfer rates. These applications have impulsed a large number of theoretical, computational and experimental research of bubbly flows, however, although these advances many complex

1877-0509
Peer-review under responsibility of the scientific committee of the International Conference on Computational Science
10.1016/j.procs.2017.05.076

problems remain unsolved [9, 12]. Hence, the primary motivation of this study is to contribute to the understanding of this type of flows.

The physical description of bubbly flows leads to a complex and highly non-linear problem. Indeed, the use of exact analytical solutions is restricted to the most simple cases, whereas the design of experiments is difficult due to limitations in optical access. On the other hand, the development of computers has promoted the combination of High-Performance Computing (HPC) and Direct Numerical Simulation (DNS) of the Navier-Stokes equations as another approach to design non-invasive experiments of bubbly flows, with accurate control of the bubble size distribution, coalescence, deformability, and flow conditions [12]. Many methods have been introduced for DNS of two-phase flows, for instance: level set (LS) methods [18, 10, 2, 3, 4, 1], volume-of-fluid (VOF) methods [15], coupled VOF/LS methods [5], and the front tracking (FT) method [11]. These approaches solve two-phase flow using the so-called one-fluid formulation, where physical properties are regularized across the dynamic interface, which is captured using a Eulerian approach (VOF, LS, VOF/LS) or a Lagrangian (FT) framework.

In the context of the methods mentioned above, [13, 5, 4] numerically studied the buoyancy-driven motion of single bubbles on unconfined domains, whereas further works on the dynamics of bubble swarms have been reported by [20, 21, 22]. Despite the fact that previous papers touched upon wall effects on single bubbles [16, 19] in square and axisymmetric ducts, employing the VOF and FT methods respectively, there are not yet computational studies of the gravity-driven motion of 3D bubbles and bubble swarms in a circular channel. Moreover, most of the previous numerical research about the dynamics of bubble swarms has been performed using the front-tracking method [11], so that the capability and accuracy of new methodologies for simulation of bubble swarms, are still to be proven. Indeed, this work aims to study the effect of the wall on the gravity-driven motion of single and multiple bubbles rising in a vertical channel, using a multiple marker CLS method introduced by [3]. Thus, using the CLS method [2, 10], the accumulation of mass conservation error inherent to standard LS formulations, is circumvented. On the other hand, the numerical and potentially unphysical coalescence of the fluid interfaces, which is inherent to CLS, LS and VOF methods, is also avoided, by means of the multiple marker CLS methodology [4]. This method can solve the interaction of multiple bubbles in the same control volume, allowing for long time simulations of bubbly flows, with a constant number of bubbles, and taken into account the bubble collisions.

The present paper is organized as follows: The mathematical formulation and numerical methods are presented in section 2. Numerical experiments are presented in section 3. Finally, concluding remarks are given in section 4.

2 Mathematical formulation and numerical methods

The mathematical model used in this work has been introduced in [3], and here is reviewed for the sake of completeness. In this formulation, the Navier-Stokes equations for the dispersed fluid in Ω_d and continuous fluid in Ω_c are written in a global domain $\Omega = \Omega_d \cup \Omega_c$, using a singular source term for the surface tension force at the interface Γ [2, 3, 1]:

$$\frac{\partial}{\partial t}(\rho \mathbf{v}) + \nabla \cdot (\rho \mathbf{v}\mathbf{v}) = -\nabla p + \nabla \cdot \mu \left(\nabla \mathbf{v} + (\nabla \mathbf{v})^T\right) + (\rho - \rho_0)\mathbf{g} + \mathbf{f}_\sigma \delta_\Gamma \tag{1}$$

$$\nabla \cdot \mathbf{v} = 0 \tag{2}$$

where p is the pressure field, $\mathbf{v}$ is the velocity, ρ is the fluid density, μ is the dynamic viscosity, $\mathbf{g}$ is the gravitational acceleration, $\mathbf{f}_\sigma$ is the surface tension force, subscripts d and c are used for the

dispersed and continuous fluids respectively, and δ_Γ is the Dirac delta function concentrated at the interface. Since a periodic domain is used in the $y - axis$ direction, the force $-\rho_0 \mathbf{g}$ is included in the Navier-Stokes equations [4], with $\rho_0 = V_\Omega^{-1} \int_\Omega (\rho_d \phi_d + \rho_c(1-\phi_d))\, dV$, to prevent the acceleration of the flow field in the downward vertical direction by the action of $\mathbf{g}$ [4, 3]. Physical properties are constant at each fluid-phase with a jump discontinuity at the interface:

$$\rho = \rho_d H_d + \rho_c(1 - H_c) \qquad \mu = \mu_d H_d + \mu_c(1 - H_c) \tag{3}$$

where H_d is the Heaviside step function that is one at fluid d and zero elsewhere. At the discretized level, a continuous treatment of physical properties is adopted to avoid numerical instabilities at the interface, according to the multiple marker CLS method [3, 1].

The conservative level-set method (CLS) [10] deployed by [2] is used in present work for interface capturing on general unstructured grids. Moreover, each fluid particle is represented by a CLS function in order to avoid their numerical merging [3, 1]. Thus, the interface of the ith fluid particle is defined as the 0.5 iso-surface of a smoothed indicator function ϕ_i, where $i = 1, 2, ..., n_d$ and n_d is the total number of bubbles in Ω_d. Since the velocity field is solenoidal, Eq. 2, the ith interface advection equation is written in conservative form:

$$\frac{\partial \phi_i}{\partial t} + \nabla \cdot \phi_i \mathbf{v} = 0 \tag{4}$$

Furthermore, an additional re-initialization equation is introduced in order to keep a sharp and constant interface profile:

$$\frac{\partial \phi_i}{\partial \tau} + \nabla \cdot \phi_i(1 - \phi_i)\mathbf{n}_i = \nabla \cdot \varepsilon \nabla \phi_i \tag{5}$$

This equation is advanced in τ up to achieve the steady state. The compressive term, $\phi_i(1 - \phi_i)\mathbf{n}_i|_{\tau=0}$, forces the CLS function to be compressed along the normal vector $\mathbf{n}_i$, whereas the diffusion term $\nabla \cdot \varepsilon \nabla \phi_i$ ensure the profile remains of characteristic thickness $\varepsilon = 0.5h^{0.9}$, with h defined as the grid size [2, 1].

Geometrical information on the interface Γ_i, such as normal vector $\mathbf{n}_i$ and curvature κ_i, are obtained as follows: $\mathbf{n}_i(\phi_i) = \nabla \phi_i / \|\nabla \phi_i\|$ and $\kappa_i(\phi_i) = -\nabla \cdot \mathbf{n}_i$. Surface tension force is calculated by the continuous surface force model [6], extended to the multiple marker CLS method in [3, 1], as follows:

$$\mathbf{f}_\sigma \delta_\Gamma = \sum_{i=1}^{n_d} \sigma \kappa_i(\phi_i) \mathbf{n}_i \delta_{\Gamma_i} = \sum_{i=1}^{n_d} \sigma \kappa_i(\phi_i) \mathbf{n}_i ||\nabla \phi_i|| \tag{6}$$

Finally, in order to avoid numerical instabilities at the interface, fluid properties in Eq. 3 are regularized using a global level-set function $H_d = \phi_d$ [3, 1], defined as follows: $\phi_d(\mathbf{x}, t) = max\{\phi_1(\mathbf{x}, t), ..., \phi_{n_d-1}(\mathbf{x}, t), \phi_{n_d}(\mathbf{x}, t)\}$.

The Navier-Stokes equations, Eq. (1-2), and interface capturing equations, Eqs. (4-5), are solved with a finite-volume discretization of the physical domain on a collocated unstructured mesh [2], where both scalar and vector variables (p, $\mathbf{v}$, ϕ, ρ, μ) are stored in the cell centroids. Following [2], the convective term of momentum Eq. (1), and interface transport Eq. (4) is explicitly computed approximating the fluxes at cell faces with a Total Variation Diminishing (TVD) Superbee limiter scheme [2]. Diffusive terms are centrally differenced, whereas a distance-weighted linear interpolation is used to find the cell face values of physical properties and interface normals. Gradients are computed at cell centroids using the least-squares method [2]. A central difference scheme is employed to discretize both compressive and diffusive terms

of the re-initialization Eq. (5). The resolution of the velocity and pressure fields is achieved using a standard fractional-step projection method originally developed by [14]:

$$\frac{\rho\mathbf{v}^* - \rho^n\mathbf{v}^n}{\Delta t} = -\mathbf{C}^n + \mathbf{D}^n + (\rho - \rho_0)\mathbf{g} + \sum_{i=1}^{n_d} \sigma\kappa_i(\phi_i)\mathbf{n}_i||\nabla_h\phi_i||, \qquad \frac{\rho\mathbf{v} - \rho\mathbf{v}^*}{\Delta t} = -\nabla_h(p) \quad (7)$$

where super-index n denotes the previous time step, $\mathbf{C} = \nabla_h \cdot (\rho\mathbf{v}\mathbf{v})$, and $\mathbf{D} = \nabla_h \cdot \mu\left(\nabla_h\mathbf{v} + (\nabla_h\mathbf{v})^T\right)$ with $(\nabla_h\mathbf{v})^T$ calculated by means of the least-squares method [2]. Imposing $\nabla_h \cdot \mathbf{v} = 0$ to the corrector step in Eq. (7) results in a Poisson equation for pressure field, which is solved by means of a preconditioned conjugate gradient method:

$$\nabla_h \cdot \left(\frac{1}{\rho}\nabla_h p\right) = \frac{1}{\Delta t}\nabla_h \cdot (\mathbf{v}^*) \qquad \mathbf{e}_{\partial\Omega} \cdot \nabla_h p|_{\partial\Omega} = 0 \quad (8)$$

Furthermore, a cell-face velocity $\mathbf{v}_f$ [2, 1] is used to advect momentum and CLS functions, in order to fulfill the incompressibility constraint in each control volume, Eq. 2, and to avoid pressure-velocity decoupling when the pressure projection is made on collocated meshes [17]:

$$\mathbf{v}_f = \sum_{q\in\{P,F\}} \frac{1}{2}\left(\mathbf{v}_q + \frac{\Delta t}{\rho_q}(\nabla_h p)_q\right) - \frac{\Delta t}{\rho_f}(\nabla_h p)_f \quad (9)$$

where P and F are the control volumes with common face f [2, 1]. A TVD Runge-Kutta method [8] is used for time integration of both advection Eq. (4) and re-initialization Eq. (5). Solving re-initialization Eq. (5) to steady-state results in a smooth transition of ϕ_i at the interface, proportional to the diffusion coefficient $\varepsilon = 0.5h^{0.9}$, where h is the grid size [2]. One iteration per physical time step of the re-initialization Eq. (5) is sufficient to keep the profile of the CLS functions in present simulations [2, 5].

Present numerical algorithms are implemented in the framework of an in-house parallel C++/MPI code called TermoFluids. The code is run on the supercomputer MareNostrum III using a range of $128 - 512$ cores for 3D simulations of both single and two bubbles, up to 2048 processors for 3D simulations of bubble swarms. The parallelization performance of the computer code implemented for the CLS method has been presented in [2], using the aforementioned supercomputer. Furthermore, the scalability of the multiple marker CLS method has been evaluated using 256 up to 1536 CPU-cores, for a system composed by 12 bubbles. The results are summarized in Table 1. The reader is referred to [2, 3, 4, 1] for technical details on the finite-volume discretization of Navier-Stokes equations, energy equation and level-set equations on collocated unstructured grids.

CPU-cores	Strong speedup	Control volumes/CPU-cores
256	1	66240
512	2.4	33120
1024	4.6	16560
1536	6.5	11040

Table 1: Parallel scalability of the multiple marker CLS method.

3 Numerical results and discussion

Extensive validations and verifications of the numerical methods are well documented in previous publications, for instance dam-break problem and buoyancy-driven motion of single bubbles

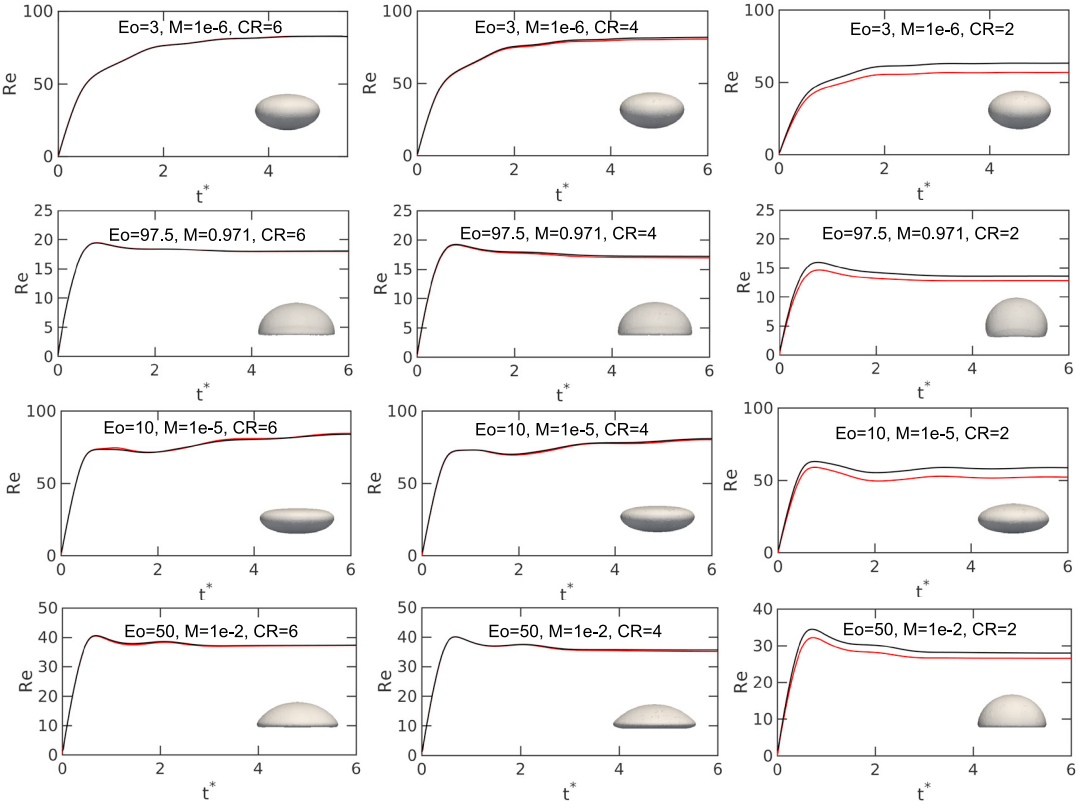

Figure 1: Effect of confinement ratio CR on Re. Single bubbles with $\eta_\rho = 100$ and $\eta_\mu = 100$. Black line for square cylinder, and red line for circular cylinder. Terminal bubble shapes in the square channel.

on unconfined domains [2, 4], drop collision against a fluid-fluid interface without coalescence [3], binary droplet collision with bouncing outcome [3], and thermocapillary-driven motion of deformable droplets [5]. Therefore, this research can be considered a further step in the understanding of wall effect on the motion of single and multiple bubbles in a vertical channel, using a multiple marker CLS approach [3].

The buoyancy-driven motion of bubbles is characterized by the Morton number $M \equiv g\mu_c^4(\rho_c - \rho_d)/(\rho_c^2\sigma^3)$, Eötvös number $Eo \equiv gd^2(\rho_c - \rho_d)/\sigma$, density ratio $\eta_\rho \equiv \rho_c/\rho_d$, viscosity ratio $\eta_\mu \equiv \mu_c/\mu_d$, and Reynolds number $Re \equiv \rho_c(\mathbf{v}_b \cdot \mathbf{e}_y)d/\mu_c$, where $\mathbf{v}_b$ is the bubble velocity, d is the initial bubble diameter, and the subscripts d and c denote the dispersed and continuous fluid phase respectively. Furthermore, the dimensionless time is given by $t^* = t\sqrt{g/d}$, whereas the confinement ratio is defined as $CR = d/D_\Omega$, with D_Ω the side length of the square section or diameter of the vertical channel.

First, the effect of confinement ratio $CR = \{2, 4, 6\}$ on the Reynolds number of single bubbles is researched, for both circular and square cylinders. Dimensionless parameters are $(Eo, M) = \{(3, 10^{-5}), (97.5, 0.971), (10, 10^{-5}), (50, 10^{-2})\}$, whereas $\eta_\rho = 100$ and $\eta_\mu = 100$ unless otherwise stated. The domain Ω is a vertical channel of size $(D_\Omega, H_\Omega) = (CR \cdot d, 10d)$, where D_Ω is the length side (square section channel) or the diameter (circular section channel), and H_Ω is

the cylinder height. No-slip boundary condition is used on the wall, and periodic boundary condition along the vertical direction ($y-axis$). The mesh is conformed by hexahedral control volumes (square section channel), or triangular-prisms (circular section channel). According to our previous work [4], the grid size $h = d/30$ is enough for capturing the dynamics of single bubbles for the range of dimensionless parameters of this work. Thus, in this research $h = d/40$ is used unless otherwise stated.

Fig. 1 shows the time evolution of Re, for circular cylinder (red line) and square cylinder (black line). The effect of the channel geometry is evident for $CR = 2$, where it is observed that Re of the circular channel is less than Re of the square channel, due the proximity of the wall to the bubble that results in an increment of the drag force. However, it is observed that the difference in Re is reduced as CR increases. According to the Grace Diagram [7], experimental Reynolds numbers (Re_{exp}) for an infinite domain are $(Eo, M, Re_{exp}) = \{(3, 10^{-6}, \sim 85), (97.5, 0.971, \sim 20), (10, 10^{-5}, \sim 88)\}$, which are close to the numerical Reynolds number (Re_{num}) calculated with $CR = 6$, as illustrated in Fig. 1. For instance $(Eo, M, Re_{num}) = \{(3, 10^{-6}, 83.1), (97.5, 0.971, 18.0), (10, 10^{-5}, 84.4)\}$ for the circular channel. Present results are consistent with numerical findings reported by [19].

3.1 Effect of the wall on the motion of two bubbles

With the aim to report numerical results of bubble swarms, the ith bubble velocity $\langle \mathbf{v}_i \rangle$, Reynolds number $\langle Re_i \rangle$ of the ith bubble, and the averaged Reynolds number of the bubble swarm $\langle Re_d \rangle$ are defined as follows [3]: $\langle \mathbf{v}_i \rangle(t) = \int_\Omega \mathbf{v}\phi_i(\mathbf{x}, t)dV / \int_\Omega \phi_i(\mathbf{x}, t)dV$, $\langle Re_i \rangle(t) = \rho_c d\langle \mathbf{v}_i \rangle \cdot \mathbf{e}_y/\mu_c$ and $\langle Re_d \rangle = (1/n_d)\sum_{i=1}^{n_d}\langle Re_i \rangle$. Where $i = \{1, 2, .., n_d\}$, and $\mathbf{e}_y$ is a unit vector parallel to $+y$ direction.

The domain Ω is a vertical square cylinder bounded by a rigid wall, with gravity in the $-y$ direction. The size of Ω is $(L_\Omega, H_\Omega) = (4d, 10d)$, where d is the initial bubble diameter, L_Ω is the square side and H_Ω is the cylinder height. Ω is discretized by 10.24×10^6 hexahedral control volumes distributed on 512 processors, whereas the grid size is $h = d/40$. As initial condition, both bubbles and liquid are quiescent. Boundary conditions are non-slip at the rigid wall and periodic on the streamwise (y-direction). Thus, bubbles go out of Ω on the top boundary, and they come back in Ω again from the opposite boundary.

Two bubbles are initially released with configuration angles $\theta_0 = \{0^o, 45^o, 90^o\}$, and centroid-centroid distance $1.5d$. Figure 2 shows the time evolution of Reynolds number, configuration angle $\theta(t)$ between $\Delta\mathbf{x}_{1,2} = \mathbf{x}_2 - \mathbf{x}_1$ and its projection on the plane $x - z$, and dimensionless separation distance between the bubbles, $s = ||\mathbf{x}_2 - \mathbf{x}_1||/d$, for $\theta_0 = \{0^o, 45^o, 90^o\}$. Due to the buoyancy force, the bubbles move upward, while bubble-bubble interaction produces oscillatory trajectories, as illustrated in Fig. 2 for $s(t)$ and $\theta(t)$. The deformable bubbles tend to move up to the wall, but they do not collide against the wall, where a bouncing effect is observed. Furthermore, θ decreases as the time advances for $\theta_0 = \{45^o, 90^o\}$, indicating that two bubbles tend to align side-by-side, due to a torque action between their centroids, as shown in Fig. 3. It is observed that a pair of deformable bubbles repel each other for $\theta_0 = \{0^o, 45^o\}$, whereas they reproduce the drafting-kissing-tumbling (DKT) phenomenon for $\theta_0 = 90^o$ (Fig. 3). In the drafting stage, the trailing bubble moves faster than the leading one, indeed, they approach closer. Then, in the kissing stage, bubbles almost touch each other and the gap between them is less than the grid size h. In the tumbling stage, a rotating effect between bubble centroids is observed, whereas the bubbles begin to separate each other, as illustrated in Fig. 3.

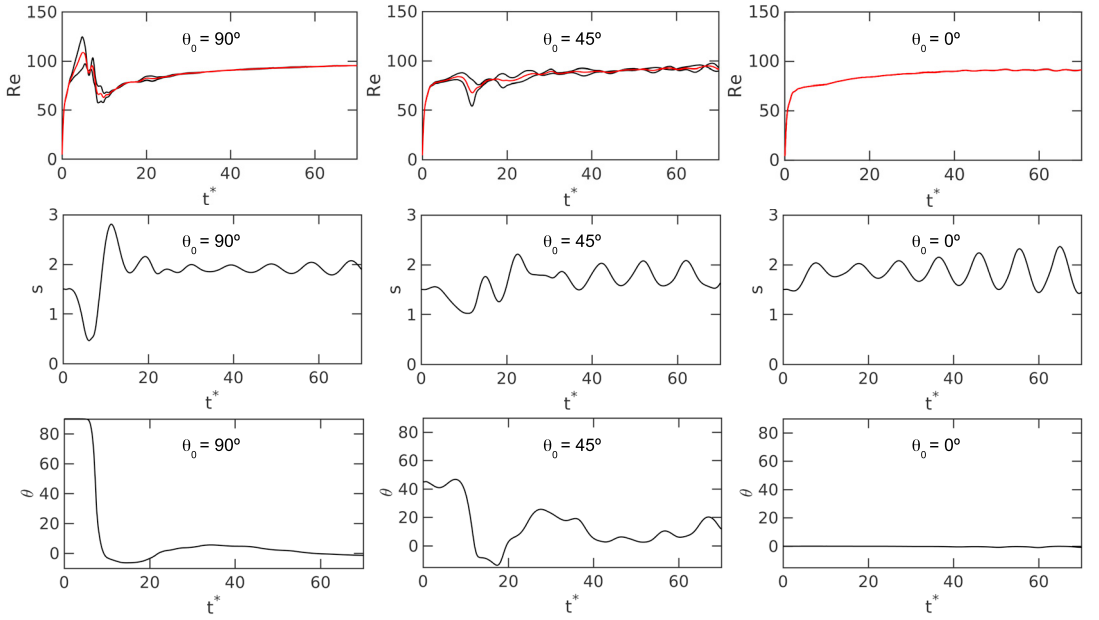

Figure 2: Interaction of 2 bubbles, $Eo = 3$, $M = 10^{-6}$, $\eta_\rho = 100$ and $\eta_\mu = 100$, $CR = 4$.

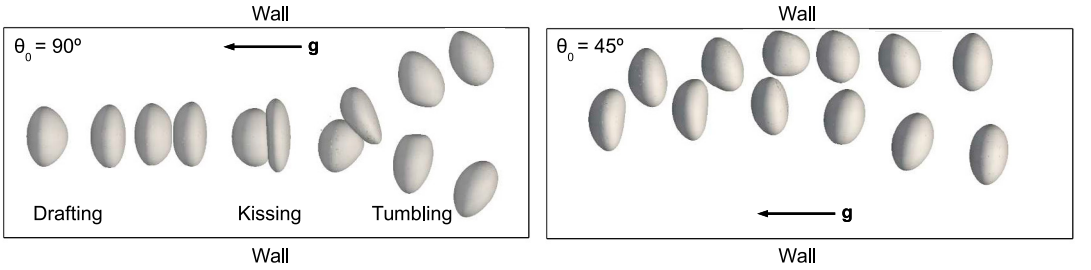

Figure 3: Interaction of 2 bubbles, $Eo = 3$, $M = 10^{-6}$, $\eta_\rho = 100$ and $\eta_\mu = 100$, $CR = 4$. $t^* = \{3.7, 5.0, 6.2, 7.5, 8.8\}$ for $\theta_0 = 90^o$, $t^* = \{8.8, 10.0, 11.2, 12.5, 13.8\}$ for $\theta_0 = 45^o$.

3.2 Effect of the wall on the motion of bubble swarms

Ω is defined as a vertical circular cylinder bounded by a rigid wall. The size of Ω is $(D_\Omega, H_\Omega) = (CR \cdot d, 4d)$, where D_Ω is the cylinder diameter and H_Ω the cylinder height. Ω is divided in 7.307×10^6 up to 16.592×10^6 triangular-prisms with grid size $h = d/40$, for $CR = 4$ and $CR = 6$ respectively, distributed on 2048 CPU-cores. Non-slip boundary condition is used on the wall, and periodic boundary condition on the streamwise (y-direction). The bubbles are initially placed in Ω following a random pattern, whereas both bubbles and liquid are quiescent. Since fluid-phases are assumed to be incompressible and coalescence of the bubbles is not allowed, the void fraction, $\alpha = V_{bubbles}/V_\Omega$, is constant throughout the simulation.

Dimensionless parameters are $Eo = 3$, $M = 10^{-6}$, $\eta_\rho = 100$, $\eta_\mu = 100$, and $(\alpha, CR) = \{(8.33\%, 6), (12.5\%, 4), (10.4\%, 4), (8.3\%, 4)\}$, corresponding to dilute bubbly flows with 18, 12, 10 and 8 bubbles. Thus, present simulations are performed with higher Reynolds numbers, as

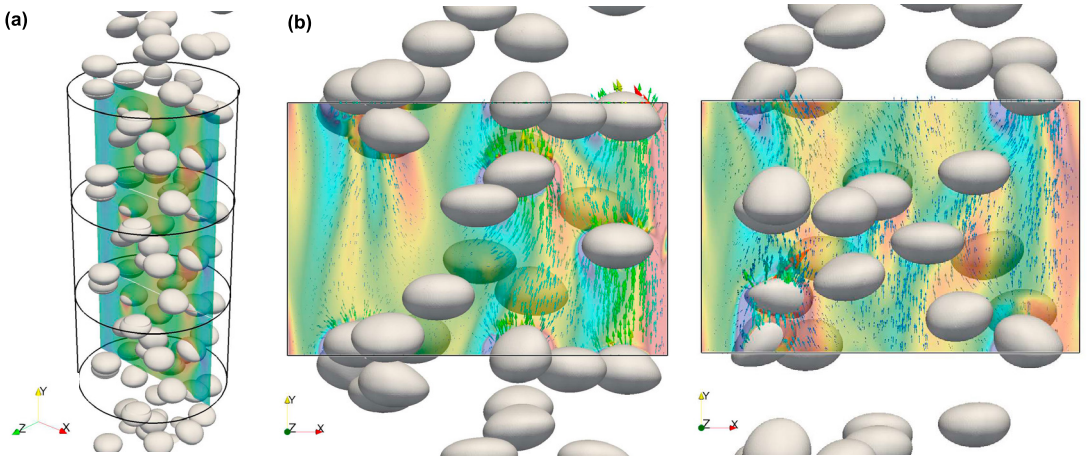

Figure 4: 18 deformable bubbles, $Eo = 3$, $M = 10^{-6}$, $\eta_\rho = 100$ and $\eta_\mu = 100$, $CR = 6$, $\alpha = 8.3\%$. (a) Vertical velocity at $z = 0$ and $t^* = 50$. (b) Vorticity $(\nabla \times \mathbf{v}) \cdot \mathbf{e}_z$ and velocity vectors, on $z = 0$ at $t^* = \{80, 103\}$.

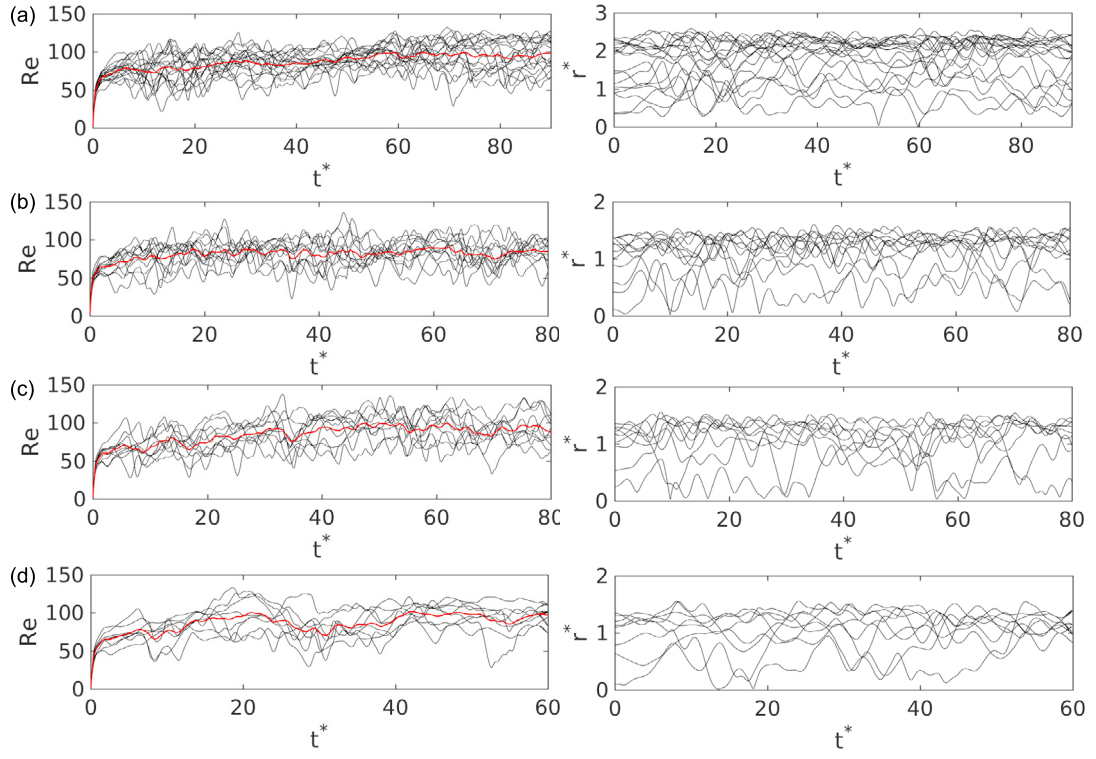

Figure 5: $Eo = 3$, $M = 10^{-6}$, $\eta_\rho = 100$ and $\eta_\mu = 100$, (a) 18 bubbles, $CR = 6$, $\alpha = 8.3\%$. (b) 12 bubbles, $CR = 4$, $\alpha = 12.5\%$. (c) 10 bubbles, $CR = 4$, $\alpha = 10.4\%$. (d) 8 bubbles, $CR = 4$, $\alpha = 8.3\%$.

well as using higher density and viscosity ratios, in comparison with our previous results [3]. Fig. 4a illustrates the motion of a swarm of 18 bubbles in a vertical column, at $t^* = 50$. Fig. 4b depicts the vorticity $\mathbf{e}_y \cdot \nabla \times \mathbf{v}$ generated by the wake interaction of the wall and bubbles, on the plane $z = 0$, for $t^* = \{80, 103\}$. Close to the wall, the vorticity generated by the bubbles has opposite sign that vorticity produced by the wall, indeed, while the velocity decreases the pressure increases in this zone, leading to a repulsion effect that avoids the collision of the bubbles against the wall. Fig. 5 shows the time evolution of Re_i for each bubble (black lines) and the averaged Re of the bubble swarm (red lines). In general, the motion of the single bubbles presents a transient behavior originated by the continued bubble-bubble and bubble-wall interactions. However, the bubble swarm achieves a quasi-steady state in all cases. Fig. 5 also depicts the radial position ($r^* = r/d$) for each bubble centroid, which indicates that bubbles tend to migrate to the wall, whereas they keep aligned at an almost constant distance without colliding against the wall. Furthermore, the interactions of the bubbles tend to follow the DKT mechanism or bouncing effect described in the previous section, consistently with front-tracking simulations reported by [21]. A comparison of Fig. 5a against Figs. 5b-d illustrate a slightly decrease of the average Reynolds number, which is a consequence of the reduction in the confinement ratio. On the other hand, Figs. 5b-d also demonstrate that for the same confinement ratio, the average Re is almost unaltered, given a void fraction $\alpha > 8\%$, with a number of bubbles above 8.

4 Conclusions

A numerical study of the wall effect on the buoyancy-driven motion of single bubbles and bubble swarms has been performed using a parallel multiple marker CLS method [3, 1]. From a numerical and computational point of view, these numerical experiments demonstrate the ability of the present method [3, 1] for the accurate simulation of bubbly flows, including bubble collisions without numerical merging of the fluid interfaces, as well as bubbly flows with high density ratio. Furthermore, the inclusion of a TVD Superbee scheme [2] to discretize the convective term of momentum equation has proved to benefit the numerical stability of the solver, avoiding numerical oscillations at the interface whereas the numerical diffusion is minimized. From a physical point of view, a repulsion effect arises from the interaction of two-bubbles in a vertical channel for $\theta_0 = \{0^0, 45^0\}$, whereas the bubbles reproduce the DKT mechanism for $\theta_0 = 90^0$. In addition, deformable bubbles tend to migrate to the wall but they do not collide with it, moreover, bubble interactions follow also the DKT behaviour in bubble swarms. This random motion of the bubbles results in a fluctuating velocity field, analogous to that observed in turbulence. Future work includes the study of pressure-driven laminar/turbulent bubbly flows, as well as the systematic introduction of variable surface tension [1], phase change, mass transfer and chemical reactions.

Acknowledgments

This work has been financially supported by the *Ministerio de Economía y Competitividad, Secretaría de Estado de Investigación, Desarrollo e Innovación* (MINECO), Spain (ENE2015-70672-P), and by Termo Fluids S.L. Néstor Balcázar acknowledges financial support of the *Programa Torres Quevedo* MINECO (PTQ-14-07186), Spain. Three-dimensional simulations were carried out using computing time awarded by PRACE 10th Call (project 2014112666) on the supercomputer MareNostrum III based in Barcelona, Spain.

References

[1] Balcázar, N., Rigola, J., Castro, J., Oliva, A., 2016. A level-set model for thermocapillary motion of deformable fluid particles. International Journal of Heat and Fluid Flow 62, Part B, 324-343.

[2] Balcázar, N., Jofre, L., Lehmkhul, O., Castro, J., Rigola, J., 2014. A finite-volume/level-set method for simulating two-phase flows on unstructured grids. International Journal of Multiphase Flow 64, 55-72

[3] Balcázar, N., Lehmkhul, O., Rigola, J., Oliva, A., 2015. A multiple marker level-set method for simulation of deformable fluid particles. International Journal of Multiphase Flow 74, 125-142

[4] Balcázar, N., Lemhkuhl, O., Jofre, L., Oliva, A., 2015. Level-set simulations of buoyancy-driven motion of single and multiple bubbles. International Journal of Heat and Fluid Flow 56, 91-107

[5] Balcázar, N., Lehmkhul, O., Jofre, L., Rigola, J., Oliva, A. 2016. A coupled volume-of-fluid/level-set method for simulation of two-phase flows on unstructured meshes. Computers and Fluids 124, 12-29

[6] Brackbill, J.U., Kothe, D.B., Zemach, C., 1992. A Continuum Method for Modeling Surface Tension, J. Comput. Phys. 100, 335-354.

[7] Clift, R., Grace, J.R., Weber, M.E., Bubbles, Drops and Particles. Academin Press, New York, 1978.

[8] Gottlieb, S., Shu, C.W., 1998. Total Variation Dimishing Runge-Kutta Schemes, Mathematics of Computations 67, 73-85.

[9] Mudde, R., 2005. Gravity-Driven bubbly flows, Annu. Rev. Fluid Mech. 37, 393-423.

[10] Olsson, E., Kreiss, G., 2005. A conservative level set method for two phase flow, J. Comput. Phys. 210, 225-246.

[11] Tryggvason, G., Bunner, B., Esmaeeli, A., Juric, D., Al-Rawahi, N., Tauber, W., Han, J., Nas, S., Jan, Y-J., 2001. A Front-Tracking Method for the Computations of Multiphase Flow, J. Comput. Phys. 169, 708-759.

[12] Tryggvason, G., Dabiri, S., Abouhasanzadeh, B., Jaicai, L., 2013. Multiscale considerations in direct numerical simulations of multiphase flows, Phys. Fluids 25, 031302.

[13] Van Sint Annaland, M., Deen, N.G., Kuipers, J.A.M., 2005. Numerical Simulation of gas bubbles behaviour using a three-dimensional volume-of-fluid method, Chemical Engineering Science 60, 2999-3011.

[14] Chorin, A.J., Numerical solution of the Navier-Stokes equations. 1968. Math. Comput. 22, 745-762.

[15] Hirt, C., Nichols, B., 1981. Volume of fluid (VOF) method for the dynamics of free boundary, J. Comput. Phys. 39, 201-225

[16] Kumar, P., Vanka, S.P., 2015. Effects of confinement on bubble dynamics in a square duct, Int. J. Multiphase Flow, 77, 32-47.

[17] Rhie, C.M., Chow, W.L., 1983. Numerical Study of the Turbulent Flow past an Airfoil with Trailing Edge Separation, AIAA J. 21, 1525-1532.

[18] Sussman, M., Smereka, P., Osher, S., 1994. A Level Set Approach for Computing Solutions to Incompressible Two-Phase Flow, J. Comput. Phys. 144, 146-159.

[19] Mukundakrishnan, K., Quan, S., Eckmann, D.M., Ayyaswamy, P.S., 2007. Numerical study of wall effects on buoyant gas-bubble rise in a liquid-filled finite cylinder, Phys. Rev. E. 76, 036308-01036308-15.

[20] Yin, X. and Koch, L., 2008. Lattice-Boltzmann simulation of finite Reynolds number buoyancy-driven bubbly flows in periodic and wall domains, Physics of fluids 20, 103304.

[21] Bunner, B., Tryggvason, G., 2002. Dynamics of homogeneous bubbly flows Part 1. Rise velocity and microstructure of the bubbles, J. Fluid Mech. 466, 17-52.

[22] Esmaeeli, A., Tryggvason, G., 2005. A DNS study of the buoyant rise of bubbles at O(100) Reynolds number, Physics of Fluids 17, 093303.